

Quantum Dynamical and isotopic effects for Hydrogen isotopes scattering at W(110) surface

Raúl Bombín,^{1,2, a)} Oihana Galparsoro,³ Daniel Peláez,⁴ Jean Christophe Tremblay,⁵ Cédric Crespos,¹ and Pascal Larregaray¹

¹⁾*Institut des Sciences Moléculaires (ISM), Université de Bordeaux, 351 Cours de la Libération, 33405 Talence, France*

²⁾*Donostia International Physics Center (DIPC), Paseo Manuel de Lardizabal 4, 20018 Donostia-San Sebastián, Spain*

³⁾*Kimika Fakultatea, Euskal Herriko Unibertsitatea EHU, Donostia-San Sebastián 20018, Spain*

⁴⁾*Université Paris-Saclay, CNRS, Institut des Sciences Moléculaires d'Orsay, 91405 Orsay, France*

⁵⁾*CNRS-Université de Lorraine, LPCT, 57070 Metz, France*

(Dated: 6 March 2026)

We investigate the scattering of hydrogen isotopes at the W(110) surface using both classical and quantum dynamics approaches to elucidate the role of quantum effects in this system. To characterize the scattering process we focus on key observables, including the absorption probability and diffraction channels that we evaluate at the quasi-classical and quantum levels. The quantum dynamics reveal pronounced resonance structures in the absorption curve that we rationalize in terms of diffraction-mediated selective adsorption and focused sticking mechanisms. Diffraction probabilities for reflected trajectories exhibit strong quantum effects at low incident energies, where classical dynamics underestimate the back scattering probability. These effects become less pronounced with increasing isotope mass, from hydrogen to tritium, however discrepancies between the classical and quantum description persist at low incident energies.

I. INTRODUCTION

Hydrogen isotopes interacting with tungsten surfaces are systems of technological relevance for nuclear fusion research. Tungsten is the prime candidate material for plasma-facing components of future fusion reactors such as ITER¹, due mainly to its high melting point. Understanding hydrogen isotopes retention, and energy dissipation mechanisms at tungsten surfaces is essential for predicting fuel recycling and material degradation under reactor operation conditions. Current large-scale experimental programs, such as WEST and JET programs, aim to understand plasma-facing components performance under steady-state operation conditions with deuterium (D) and tritium (T)²⁻⁴. This efforts have been accompanied by theoretical *ab-initio* studies of deuterium trapping at tungsten dislocations⁵ and investigations of fuel retention at high energies⁶.

The latter has motivated also fundamental research on this system from a microscopic perspective with the aim of obtaining insight into the macroscopic phenomena. Several works based on chemically accurate potential energy surfaces (PES) established a detailed description of H₂ interacting with W(110)⁷. Furthermore, subsequent studies considering atomic scattering have demonstrated the crucial role that non-adiabatic effects play in the absorption dynamics, being specially important the energy dissipation due to the creation electron-hole pair excitations in the metal. The latter is modeled by Langevin dynamics simulations including friction and stochastic forces^{8,9}, and has been successful in reproducing experimental observations for atomic scattering on fcc metallic surfaces^{10,11}. These research have been extended to analyze the effects of hydrogen surface coverage and of incident

angle on energy-loss distributions^{12,13}. Alternative descriptions based on effective medium theory were also applied to BCC metals, including tungsten¹⁴. The previous studies have been done in low dimensional PES, but, more recently multidimensional machine-learning PES studies have examined coverage and isotopic effects in the H/W system¹⁵. Similarly, hydrogen scattering on the more open W(100) surface has also attracted considerable attention^{13,16,17}. The mentioned works for the tungsten surfaces complement other studies in the bibliography for other transition-metal surfaces^{11,18}. All in all atomic scattering on metal surfaces have revealed itself as a reference system in which to benchmark theoretical models with accurate experimental measurements¹⁹.

Due to the small mass of hydrogen atoms, quantum effects are expected to be important, this has motivated in the past the study of H₂ scattering at metal surfaces by time-dependent wave-packet (TDWP) method. Early quantum treatments employed reduced-dimensionality models, in two and three dimension, for hydrogen recombination on graphite²⁰, H₂ scattering on Cu(111)^{21,22} and Pt(111)²³. A review of six-dimensional (6D) quantum studies can be found in Ref. 24, and more recent approaches for Pt(111)²⁵, Pd(111)²⁶, and Cu(111)²⁷. Remarkably, very recently, the Eley-Rideal recombination of hydrogen atoms on Cu has been studied by TDWP in a 6D PES^{28,29}. Concerning atomic scattering, quantum studies are more scarce. The scattering of hydrogen on graphene has been explored by means of TDWP using the multi-configurational time-dependent Hartree (MCTDH) approach^{30,31}, complementing previous semi-quantum approaches using ring-polymer molecular dynamics^{32,33} on the same system. In what respect to metal surfaces, Lepetit *et al.*³⁴ studied low energy scattering at the van-der-Walls well of graphite by TDWP. However no studies have addressed the more strongly interacting case that represents the scattering at incident energies that allow to explore the chemisorption well at the metal surface. MCTDH has been applied to the graz-

^{a)}Electronic mail: raul.bombin@u-bordeaux.fr

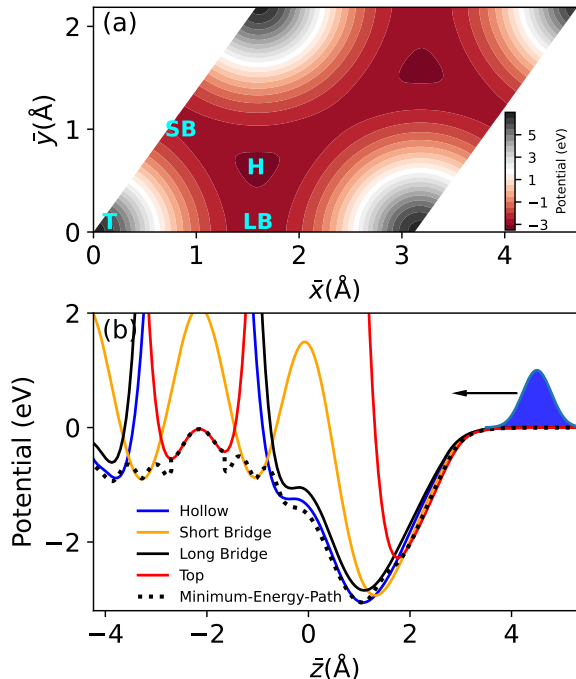


FIG. 1. (a) 2D potential energy surface cut for H/W(110) system at a distance $z = 1.1 \text{ \AA}$ from the surface. Four high-symmetry positions are labeled: Hollow (H), short-bridge (SB), long-bridge (LB) and top (T) sites. (b) Z-cuts of the PES at the high-symmetry positions. Here \bar{x} , \bar{y} and \bar{z} are orthogonal cartesian coordinates. The potential energy along the minimum energy path in shown in dotted black line.

ing incident fast-atom diffraction on semiconducting surfaces (GIFAD) of He Li(0001)^{35,36} and KCl³⁷, showing reasonable good agreement with exact wave packet results. Note however that these works consider high energy projectiles with energies in the range of kiloelectronvolts, far from the energies considered in the other works motivated by catalysis. Here we address that problem for the case of H scattering on the W(110) surface using quantum TDWP based on MCTDH approach.

The paper is organized as follows, in section II we detail the methodology that we use to conduct the classical and quantum dynamical simulations. Results are presented in section III and finally some conclusions are summarized in section IV. In appendix A the vibrational spectra of hydrogen isotopes is discussed.

II. METHOD

A. Potential Energy Surface

Classical trajectories (CT) and TDWP calculations are performed by propagating the system on a potential energy surface (PES). We make use of the Born–Oppenheimer static surface (BOSS) model, in which energy dissipation to the surface vibrations is neglected. The latter is justified by the large mis-

match between H and W masses ($m_H/m_W = 1/183.5$), which is expected to make phonon excitations negligible at low surface temperatures and for the low incident energies considered in this work, $E_{in} < 1 \text{ eV}$. Our model intentionally neglects also the energy dissipation towards the electrons at the surface. Its theoretical treatment in the quantum framework remains challenging^{38–41} and object of intense research at present. We defer this point for future research. The objective of the present work is the evaluation of the importance of quantum effects in the scattering of H at a W(110) model surface.

The PES^{42,43} is based on density functional theory calculations performed with the PW91 exchange correlation functional that relies on the generalized gradient approximation. To interpolate the PES, we employ the corrugation-reducing procedure (CRP)^{7,44,45}, which has been widely applied in studies of atomic and diatomic molecular scattering on various metal surfaces²⁴. To propagate the wave packets on the PES, we use the MCTDH method, as implemented in the Heidelberg package⁴⁶, which reduces the computational cost of quantum calculations by representing the wave function as a sum of Hartree products of nuclear orbitals. To fully exploit this approximation and maximize computational efficiency, the PES must also be expressed in separable form. A sum-of-products representation is obtained using the POTFIT program⁴⁷ included in the Heidelberg package. Further details about the POTFIT procedure are given in section II C.

Although the CRP method is able to describe a 6D potential for a diatom interaction with the surface, here we consider single atom scattering, thus the potential is a three dimensional (3D) function of the position of the atom, $V^{3D}(x, y, z)$. In the choice of coordinates, the XY plane is parallel to the surface and the Z direction is perpendicular to it, with $z = 0$ corresponding to the height of the topmost layer of W atoms. The X and Y axes coincide with the W(110) surface’s cell skewed lattice vectors, that form an angle $\gamma = 54.735^\circ$ between them, being the lattice constant 3.17 \AA . The symmetry of the surface is illustrated in Fig 1(a) by a PES cut in the XY plane. The height of the cut has been chosen to coincide with the equilibrium position of an H atom adsorbed on the tungsten surface ($z = 1.1 \text{ \AA}$), that is, at a hollow site. The black regions represent the repulsive barriers that exist on tungsten atop positions at this height, while the adsorption site is signaled by the dark red region, with an adsorption energy $E_{ads} \sim -3.1 \text{ eV}$. Fig. 1(b) depicts one-dimensional cuts of the PES along Z-direction for the high-symmetry positions that are labeled in panel (a): hollow, short-bridge, long-bridge and atop sites, all of them exhibiting local energy minima with increasing energy. Notice however that the latter one do not corresponds to local minima on the 3D PES but to a saddle point. In addition, the potential energy cut along the minimum energy path for absorption, calculated using the nudged elastic band (NEB) method⁴⁸, is represented by the dashed curve. As it can be seen, our PES is able to describe the system for gas phase configurations ($z > 5 \text{ \AA}$) as well as bulk penetration up to a depth of (-4.5 \AA). As atoms arrive to the surface from the gas phase, they encounter barriers at the different high-symmetry sites, lying in the range $z \in [-2.0, 1.5] \text{ \AA}$, from where they are either reflected or deflected. For small values of the incident

energy E_{in} , in order to penetrate to the bulk region, an hydrogen atom should first penetrate the surface through hollow or long-bridge positions and then follow a trajectory over short bridge, top and long bridge (hollow), iteratively. A minimum energy path, following such type of trajectory in depicted with dotted black line in Fig. 1(b).

B. Classical trajectory simulations

In the CT calculations, the nuclear motion of the hydrogen isotope is described by solving Newton's second law,

$$m_i \ddot{\mathbf{r}}_i = -\frac{dV^{3D}}{d\mathbf{r}_i}, \quad (1)$$

where V^{3D} is the adiabatic PES, and m_i , \mathbf{r}_i , and $\ddot{\mathbf{r}}_i$ denote the mass, position, and acceleration of the isotope $i = \text{H, D, T}$.

Normal incidence scattering is simulated sampling the initial in-plane coordinates of the projectile atom (x, y) are randomly sampled in a reduced section of the unit cell, taking advantage of the symmetry. The initial altitude of the projectile is $z_0 = 7.0 \text{ \AA}$, which corresponds to the asymptotic region of the atom-surface interaction potential. Our model does not consider energy dissipation to the surface degrees of freedom, thus, there are two possible exit channels for the simulations: absorption in the bulk and reflection. An atom is considered reflected when it reaches its initial height z_0 and it is considered to be absorbed when it crosses the plane located at $z = -2.5 \text{ \AA}$. Notice that for short propagation times, dynamical trapping occurs at the surface. For the results presented here, trajectories are propagated to long enough times so that the dynamical trapping probability vanishes. At the lowest incident energy considered ($E_{\text{in}} = 10 \text{ meV}$), propagation times of up to 20 ps are required. To reach convergence for the absorption curves, 1000 trajectories are performed for each value of the incident energy, while to obtain converged results for the diffraction patterns up to 8 million classical trajectories are run for each case.

C. Wave packet simulations

The state of the system is represented as a wave packet, $\Psi(X, Y, Z; t)$, that evolves according to the time-dependent Schrödinger equation

$$i\hbar \frac{\partial \Psi(X, Y, Z; t)}{\partial t} = \hat{H} \Psi(X, Y, Z; t) \quad (2)$$

The Hamiltonian, \hat{H} , describing the interaction of an atom of mass M with a frozen surface is given by

$$\hat{H} = -\frac{\hbar^2}{2M \sin^2 \gamma} \left[\frac{\partial^2}{\partial^2 X} + \frac{\partial^2}{\partial^2 Y} - 2 \cos \gamma \frac{\partial}{\partial X} \frac{\partial}{\partial Y} \right] - \frac{\hbar^2}{2M} \frac{\partial^2}{\partial^2 Z} + V^{3D}(X, Y, Z). \quad (3)$$

where we have employed non-orthogonal, skewed coordinates $\{X, Y, Z\}$, which are related via the skewing angle $\gamma = 54.735^\circ$

to the Cartesian ones, $\{\bar{x}, \bar{y}, \bar{z}\}$, by the relations

$$X = \bar{x} - \bar{y}/\tan(\gamma) \quad ; \quad Y = \bar{y}/\sin(\gamma) \quad ; \quad Z = \bar{z}. \quad (4)$$

To perform the time-dependent wave-packet calculations, we rely on the MCTDH method as implemented in the Heidelberg package. The wave function that describes the time-evolution of the systems is expanded as a sum of Hartree products of single particle functions (SPFs), that in our 3D case reads

$$\Psi(X, Y, Z; t) = \sum_{j_x=1}^{n_x} \sum_{j_y=1}^{n_y} \sum_{j_z=1}^{n_z} A_{j_x j_y j_z}(t) \varphi_{j_x}(X, t) \varphi_{j_y}(Y, t) \varphi_{j_z}(Z, t). \quad (5)$$

Here, $A_{j_x j_y j_z}(t)$ are time-dependent expansion coefficients. A number n_i of SPFs $\{\varphi_{j_i}\}$ is chosen to represent accurately the $Q_\kappa = \{X, Y, Z\}$ nuclear degree of freedom. In the Heidelberg implementation of MCTDH, the SPFs for the generalized Q_κ coordinates are further expanded in a time-independent primitive basis of functions $\{\chi_{i_\kappa}(Q_\kappa)\}$ as

$$\varphi_{j_\kappa}(Q_\kappa, t) = \sum_{i_\kappa=1}^{N_\kappa} c_{i_\kappa j_\kappa}(t) \chi_{i_\kappa}(Q_\kappa), \quad (6)$$

with $c_{i_\kappa j_\kappa}(t)$ the time-dependent coefficients of the SPF and N_κ the number of grid points associated to the κ -th degree of freedom. Substituting Eq. (5) in Eq. (2) and applying the Dirac-Frenkel variation principle leads to coupled equations of motion (EOM) for the coefficients, $A_{j_x j_y j_z}(t)$, and the SPFs, via the evolution of the contraction coefficients $c_{i_\kappa j_\kappa}(t)$. These EOM can be solved numerically using various integration schemes, as described in detail elsewhere⁴⁶. Here, we make use of the so-called constant mean-field integration (CMF) scheme (relative tolerance: 10^{-5}), using the Burlisch-Stoer algorithm (steps: 7, relative tolerance: 10^{-7}) and Short-Iterative Lanczos algorithm (iteration depth: 12, relative tolerance: 10^{-6}) for the propagation of the SPFs and coefficients, respectively. Although the Hartree wave function of Eq. (5) does not account exactly for nuclear quantum correlation effects, the multi-configurational nature of the MCTDH ansatz accounts for dynamical correlation between the different degrees of freedom induced by the corrugation of the potential energy surface. To correctly describe this nuclear correlation, the convergence of the SPF basis with respect to $\{n_x, n_y, n_z\}$ was carefully checked. Table I summarizes the parameters used in the calculations for the different isotopes. Note that a larger number of SPFs is needed to obtain converged results

TABLE I. Number of SPFs, n_κ , per degree of freedom, $Q_\kappa = \{X, Y, Z\}$, for the MCTDH calculations used in this work for the simulation of H, D and T scattering on the W(110) surface.

isotope	n_x	n_y	n_z
H	50	50	100
D	61	54	105
T	65	56	110

for heavier isotopes. This seems contradictory with the observation that quantum effects are less pronounced in heavier atoms. Nevertheless, this can be understood by the fact that the same potential wells support more bound states for heavier isotopes. Thus, a larger basis is needed to model the intermediate scattering states for a given value of the incident energy. As a consequence, there is a sharp increase in the computational cost upon an increase in the isotope mass.

Throughout this work, we use the Fast Fourier Transform (FFT) periodic collocation method for the primitive basis. The SPFs are represented using $N_x = 67$ points on the interval $[0, 3.170] \text{ \AA}$, $N_y = 58$ points on the interval $[0, 2.745] \text{ \AA}$, and $N_z = 316$ points on the interval $[-4.445, 7.832] \text{ \AA}$. The grid spacing, ΔQ_κ , is $4.7 \times 10^{-2} \text{ \AA}$ along X and Y , and $3.9 \times 10^{-2} \text{ \AA}$ for Z . This spacing is sufficient to resolve the highest momentum ($k_{\max}^Q = \hbar/\Delta Q_\kappa$) of the particle as it enters in the potential wells at the surface, which is limited by the impinging energy and the potential depth, i.e., a kinetic energy of $E_k \approx E_{\text{in}} + 3.1 \text{ eV}$. As required by MCTDH, in all simulations, the PES has been represented on the primitive grid in the so-called sum-of-products form using the⁴⁷. The sum of products is constructed using 63, 51 natural potentials for the X , Y degrees of freedom, and 110 for Z . This gives place to root mean square error of 4 meV. This difference in the number of potential basis functions responds to the unbound nature of the last degree of freedom.

The initial wavepacket in all of the simulations has been prepared as a Hartree product of constant functions ($k = 0$ plane waves) for the $\{x, y\}$ degrees of freedom and a complex-valued Gaussian function for the z degree of freedom. The initial width of the Gaussian is chosen as $\sigma = 0.42 \text{ \AA}$ and centered at $Z_0 = 4.76 \text{ \AA}$, with variable initial momentum p_0 defined from the incident energy E_{in} of the particle in gas phase. To avoid artificial reflections on the borders of the box along the Z direction, two Complex Absorbing Potentials (CAP) have been placed at $Z_{\text{ref}}^{\text{CAP}} = 5 \text{ \AA}$ and $Z_{\text{abs}}^{\text{CAP}} = -2.5 \text{ \AA}$ for the reflection and the absorption channels, respectively. The form of the CAP is taken as $V_0^{\text{CAP}} = -iV_0^{\text{CAP}} \theta(\pm(z - z^{\text{CAP}}))(z - z^{\text{CAP}})^2$ with the plus (minus) minus sign for the reflection (absorption) channel. The isotope and E_{in} dependent values of V_0^{CAP} are listed in Table II. To analyze the results, we compute the flux that crosses the CAPs, which gives access to absorption and reflection probabilities. To obtain the diffraction patterns, the flux that crosses the reflection channel is projected onto the diffraction states. For state-resolved analyses, bound vibrational states have been obtained from imaginary time propagations of an initial wave packet localized in the

vicinity of the surface. To this end, we employ the improved relaxation algorithm,⁴⁹ using a CMF integration scheme with an 8th order Runge-Kutta algorithm for the propagation of the SPFs and a Davidson diagonalization for the A-coefficients.

III. RESULTS

A. Absorption curve

First, we investigate the absorption and reflection probabilities for hydrogen atoms scattering at the W(110) surface. We consider the range of incident energies $E_{\text{in}} \in [0.01, 1.2] \text{ eV}$ that goes from the low energy regime, where quantum effects are expected, to the intermediate one that overlaps with the one of interest for catalysis application. We perform both classical and quantum dynamical calculations in order to characterize the regime in which quantum effects become important and identify a limit to such regime in terms of E_{in} , hereinafter, the classical limit. Above the classical limit, classical dynamics can be safely used to describe the dynamics of the system. We restrict our study to normal incidence. Furthermore, in the present work dissipation of energy is not considered and thus surface adsorption can only occur as a transient phenomena. In turn, this means that for converged calculations in terms of propagation time, the only two possible exit channels are reflection and bulk absorption. Figure 2 depicts the computed absorption (P_{abs}) and reflection (P_{ref}) probabilities as a function of energy. Classical (quantum) results are shown in dotted (solid) lines. Since $P_{\text{ref}} = 1 - P_{\text{abs}}$, only the absorption results are commented.

Attending to the classical results, one can identify three regimes in terms of E_{in} . Below $E_{\text{in}} = 200 \text{ meV}$, the absorption probability decreases as E_{in} increases. From $E_{\text{in}} = 200 \text{ meV}$ it remains essentially constant and then it starts to grow for $E_{\text{in}} > 1 \text{ eV}$. To understand the behavior at low values of E_{in} , it is necessary to consider the absorption mechanism itself. For an incident atom to penetrate into the bulk region and contribute to the absorption probability, it must transfer part of its initial energy in the Z degree of freedom, E_z , to the parallel components (X and Y). This process is illustrated by the minimum energy path shown in Fig. 1(b). This occurs naturally on a corrugated PES where trajectories are continuously deflected as they approach the surface, leading to a transient dynamical trapping. From this transient state, atoms can either be reflected back to the gas phase or penetrate to the bulk. In the former case, atoms in the transient trapping state, need to put enough energy back into the Z degree of freedom to escape the surface. For small values of E_{in} , the transient dynamical adsorption state has a long lifetime, as the atom needs to put almost all its kinetic energy on the Z degree of freedom in order to leave the surface. For this reason, the smaller E_{in} , the longer the time an atom has to explore the PES, and, eventually, to find the path towards the bulk region. This enhances the absorption probability as E_{in} is reduced. On the contrary, for $E_{\text{in}} > 1 \text{ eV}$, P_{abs} increases with the incident energy, as atoms have enough energy to overcome the energy barriers that are present at the surface. In the intermediate regime the

TABLE II. V_0^{CAP} values used for MCTDH simulations for H, D, and T depending on their initial incident energy.

V_0^{CAP}	E_{in} range (eV)		
	H	D	T
8×10^{-5}	[0.01, 0.07)	[0.01, 0.10)	[0.01, 0.23)
2×10^{-4}	[0.07, 0.75)	[0.10, 0.60)	[0.23, 0.90)
4×10^{-4}	[0.75, 1.10]	[0.60, 1.10]	

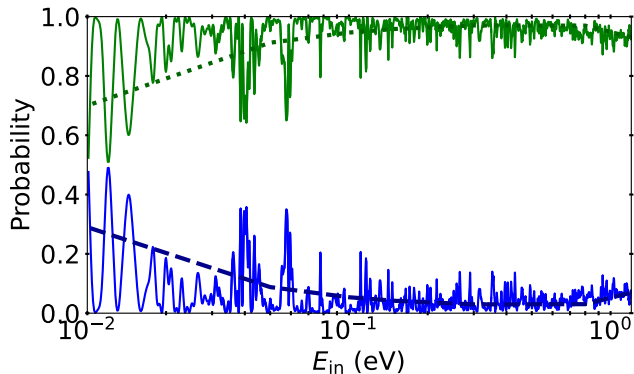


FIG. 2. Reflection (green) and absorption (blue) probabilities for H atoms scattering at W(110) surface with normal incidence as a function of incident energy E_{in} . Dashed (solid) lines correspond to classical (quantum) results.

two effects compete: the dynamical trapping, whose lifetime decreases with E_{in} , and the ability to overcome the PES barriers, that is favored for larger values of E_{in} . The competition gives rise to the region of almost constant absorption probability in terms of E_{in} ($P_{abs} \approx 5\%$).

Our results qualitatively match those of Ref. 15 for large values of the incident energy. However they disagree for lower values of E_{in} . The discrepancy arises because the simulations in Ref. 15 are stopped at $t = 1$ ps, which is too short for $E_{in} < 1$ eV when energy dissipation is neglected, as in the present case. It is interesting to compare our classical dynamics results for the W(110) surface with those presented in Ref. 16 for the W(100). The W(100) surface is rougher compared to W(110), which is a close-packed surface. On the more open W(100) surface, absorption increases as the energy decreases below 200 meV. For instance, at $E_{in} = 100$ meV, $P_{abs}^{W(100)} \approx 0.35$, which is 3.5 times larger than the corresponding value for the W(110) surface.

Fig. 2 also depicts quantum dynamical predictions, obtained with the MCTDH method, for the absorption as a function of the incident energy. At odds with the classical curve that is a smooth function of E_{in} , the curve presents oscillations due to different mechanisms: interference⁵⁰, diffraction⁵¹ and resonances due to the presence of bound states at the surface⁵¹⁻⁵³. For incident energies exceeding 150 meV, quantum and classical results become closer, consistent with a transition to the classical regime. For the largest energies studied here, however, small resonances persist, introducing minor discrepancies between the classical and quantum predictions for certain values of E_{in} . Eventually, for incident energies much larger than the scale of energy bound states in the system, the quantum curve would smooth to the classical one. Note, however, that the potential wells are of about 3 eV (see Fig. 1) and that reaching incident energies much larger than that value is computationally expensive for the necessity of using denser grid (and huge SPF basis) to represent high momentum states, which is beyond the scope of this work. More interestingly, for $E_{in} < 100$ meV the discrep-

ancies between classical and quantum results are larger. In this region, two features allow to distinguish the classical and quantum predictions. First, there is an overall overestimation of P_{abs} by the classical approach. As commented before, in order to have a finite P_{abs} , it is necessary to transfer energy to the X and Y degrees of freedom when the atom is at the surface. However, the density of available states in the quantum case is discrete, meaning that less final states are available for this purpose compared to the classical picture. This gives rise to a reduced quantum absorption probability, as a larger portion of the wave packet is directly back-scattered. This point is further disused together with the diffraction patterns in section III C. The second remarkable feature of the quantum absorption curve is the emergence of sharp resonances for $E_{in} < 100$ meV that can rise the absorption probability up to values of 50%. Note that the incident energies scale is logarithmic, and thus, the low energy resonances that seem broader in the plot are indeed narrower than those at high values of E_{in} .

Identifying all the resonances in the absorption curve is a nearly impossible task as different mechanism overlap giving rise to its complicate shape. However it is possible to identify some of them in certain intervals of E_{in} . Resonances in elastic scattering emerge due to processes that transfer energy from the incident coordinate to the other degrees of freedom. In the case of atomic scattering on a rigid surface, as in the present work, this energy transfer, ΔE , can only from the normal to the parallel degrees of freedom of the incident atom⁵². For a certain mechanism giving place to given ΔE , it must be accomplished $\Delta E = E_{in} + |E_b^j|$, with E_b^j the energy of the j -th bound state at the surface. That means that the energy transfer between the perpendicular and parallel degrees of freedom has to coincide with the sum of the incident energy plus the binding energy of a given state j at the surface. In our case, the potential for H on W(110) is deep, with a large density of bound states below $E = 0$, hence enabling a large amount of possible resonances. This means that each mechanism discussed below gives rise to signals in the interval of incident energies $(0, \Delta E)$ which correspond to coupling with bound states with binding energies $E_b \in (-\Delta E, 0)$. In the context of semi-classical theory, resonances emerge as a consequence of the existence of periodic allowed orbits⁵⁴.

In this respect, several mechanisms have been described in the literature that give rise to peaks in the absorption probability, such as the diffraction-mediated selective adsorption (DMSAR)⁵¹⁻⁵³ and the selective adsorption resonance (SAR)^{53,55,56}. To disentangle these mechanisms, we follow previous work in assuming that the intermediate state to which the incident wave packet couples can be approximately described in separable form, that is, $\Psi(X, Y, Z) \simeq f(X)g(Y)h(Z)$. In the DMSAR mechanism, the energy transfer between the Z and $\{X, Y\}$ degrees of freedom of the incident wave packet occurs through a diffraction process. The first order diffraction process for H impinging on W(110) corresponds to $\Delta E \approx 12$ (16) meV for the X (Y) directions. Fig. 3(a) depicts the absorption curve of hydrogen on W(110) for $E_{in} < 400$ meV. The golden vertical lines mark the energy of the four lowest allowed diffraction processes. Based on the

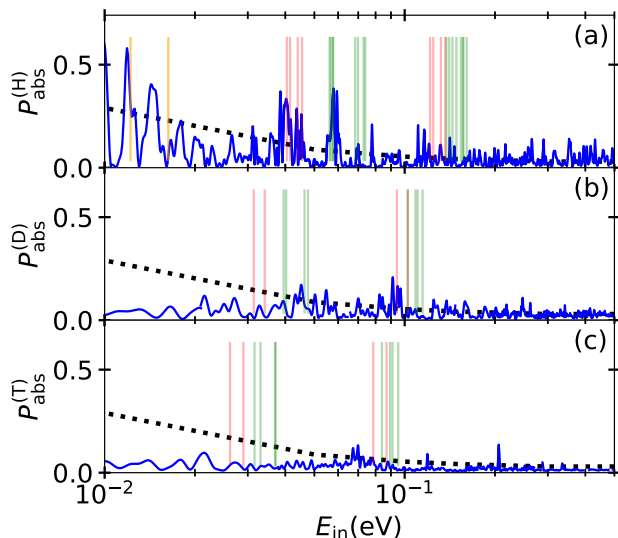


FIG. 3. Absorption probability as a function of the incident energy computed with MCTDH (solid blue line) and classical (dotted black line) methods for (a) hydrogen, (b) deuterium and (c) tritium isotopes. Vertical lines mark the energy transfer to XY degrees of freedom due to DMSAR (gold) and SAR (red) processes and combinations of them (green)

previous discussion of the classical results, these are likely responsible for the resonance structure that is observed for $E_{\text{in}} \lesssim 20$ meV. While for the DMSAR mechanism a corrugated potential is the only ingredient needed, a more spectacular resonance effect can occur, called SAR or focused sticking^{52,53}, if the potential supports also bound states. In this case, it is possible to interchange energy between the perpendicular and transversal degrees of freedom of the incident atom at channels that are forbidden by diffraction, when bound states are present in the surface for the perpendicular degrees of freedom. In Fig. 3, panels (a)-(c), red vertical lines mark the energies corresponding to bound states of H/D/T atoms at the hollow adsorption position of the W(110). For increasing energy, they correspond to the zero point energies and excitations with one vibrational quantum in the X and Y degrees of freedom (see appendix A, for more details). Starting with H [see panel (a)], the energies of its vibrational spectra at W(110) surface help to explain the resonances appearing around values of $E_{\text{in}} \sim 40$ meV and ~ 125 meV. Here we do not use the equal sign as the actual resonances arise from the coupling to the eigenstates of the full Hamiltonian. Finally, processes involving DMSAR in one of the degrees of freedom and SAR in the other one are also possible. In the figure, the energy of such processes is marked by green lines and help to explain the resonances that appear around $E_{\text{in}} = 70$ meV (high intensity) and 140 meV (weak intensity). Note that only XY bound states for the most stable position of H at the surface have been considered. However, the PES supports more transversal bound states, e.g. localized at SB and LB high-symmetry positions, that add complexity to the resonance structure that is observed in that range of energies.

The above-mentioned quantum effects arise due to the

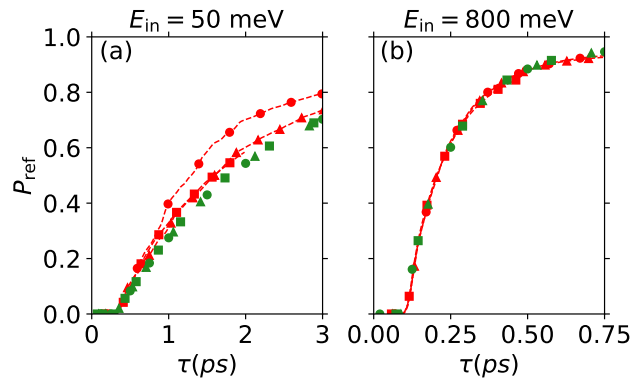


FIG. 4. Time resolved cumulative reflection probability for hydrogen (circles), deuterium (triangles) and tritium (squares) computed with MCTDH (green) and classical (red) methods. The incident energy in (a) (b) panels is 50 and 800 meV, respectively. The time on the abscissa is scaled as $\tau = t \sqrt{m_{\text{H}}/m_i}$ with $i = \text{H, D, T}$. Lines are guides to the eye.

small mass of hydrogen. One may wonder, thus, whether they will persist if one considers the heavier isotopes of hydrogen. Moreover, if the resonance mechanisms described above are correct, they should also appear for D and T. Note that the diffractive energies for D and T scale as m_{H}/m_i , while the vibrational ones scale approximately with $\sqrt{m_{\text{H}}/m_i}$ (see appendix A), with $i = \text{D, T}$. In Fig. 3 the absorption probability as a function of E_{in} for H, D and T is shown in panels (a), (b) and (c), respectively. The first thing that one can observe is that, due to the larger density of states at the surface for D and T, they approach faster to the classical limit in terms of E_{in} : what is reflected in a smoother curve for the higher incident energies. The region where the QD results are similar to the classical behaviour is displaced to lower values of E_{in} as mass increases. For the case of H, differences in the absorption probability between the classical and quantum methods larger than 10% appear for $E_{\text{in}} < 180$ meV. For deuterium such large differences appear only for $E_{\text{in}} < 100$ meV. Finally for the case of T, clear deviations between the classical and quantum predictions appear only for values of the incident energy lower than 70 meV. Further, the expected diffraction resonances for D and T appear at very low energies, which renders their computation difficult. On the other hand, SAR processes as well as their combination with DMSAR seem to compose the regions where resonances are stronger for both D and T.

Despite the above mentioned analysis, it is worth noting, however, that discrepancies at very low E_{in} persist, with the classical prediction overestimating the absorption probability. This confirms, as alluded before, that it is more difficult to transfer energy between perpendicular and parallel degrees of freedom in the quantum case compared to the classical one, which is intimately related to the reduced density of states at the surface in the quantized case. This is quite evident for T, whose absorption probability in the region $E_{\text{in}} \in [35, 70]$ meV, where no resonances are seen or expected, and the classical

prediction deviates from the quantum one.

B. Dynamical isotopic effects

Further insight into isotopic effects is obtained by analyzing the time evolution of the scattering probability. It is worth noting that for an atom moving adiabatically in an external potential, as in our model, isotopic effects have a purely quantum origin. In the classical picture, H, D, and T follow exactly the same trajectory in coordinate space if they start with the same initial conditions. The only difference is that isotopes with larger mass move slower. Indeed, the dynamics of the system for different isotopes is equivalent if it is reported using the scaled time $\tau = t\sqrt{m_H/m_i}$ with $i = H, D, T$. This is illustrated in Fig. 4, which shows the classical time evolution (green symbols) of the reflection probability as a function of the scaled time. The time evolution of P_{ref} for the three isotopes collapses onto a single line, both at low ($E_{\text{in}} = 50$ meV) and high ($E_{\text{in}} = 800$ meV) incident energies. The latter leads to the absence of isotopic effects in reflection probabilities in terms of real propagation time for the classical case.

In contrast, the quantum description introduces isotope-dependent behavior through the mass dependence of the wave-packet propagation. Being a purely quantum effect, it is expected to be more important for low values of E_{in} , consistent with the previous analysis of the absorption curves. In Fig. 4(a), the quantum evolution of P_{ref} in terms of the scaled time is shown. Results in this case are integrated over the energies of a wave packet whose translational energy is E_{in} . As can be seen, isotopic dynamical effects appear for low values of the incident energy, which makes the dynamics of H different from that of D and T. These two latter isotopes exhibit behavior that is barely distinguishable between them and that is close to the classical limit. It is worth noticing that the isotopic effect on $P_{\text{ref}}(t \rightarrow \infty)$ (averaged over wave-packet energies) is small, even in the quantum case. Remarkably, for $E_{\text{in}} = 800$ meV, quantum signatures are suppressed and, thus, isotopic differences diminish, and the average evolution of the quantum system converges toward the classical behavior. This shows that our quantum dynamical calculations approach correctly to the classical limit, which also validates their quality.

C. Diffraction patterns

Additional information about the origin of the quantum and isotopic effects that appear for low values of E_{in} is obtained from the analysis of the diffraction patterns in the reflection channel. Classically, the diffraction patterns are evaluated by introducing Gaussian binning to the reflected states in the reciprocal space, with Gaussian centered at the values of the quantum-allowed diffraction channels. In this sense, they are semi-classical⁵⁷. In MCTDH, quantum diffraction patterns are obtained by projecting the flux crossing the reflection CAP onto the corresponding diffraction states, as described in Section II.

Fig. 5 shows the probabilities associated with diffraction energy channels of energy E_{XY} . The semi-classical prediction for H, D, and T as a function of E_{XY} is reported for three different values of the incident energies: specifically, $E_{\text{in}} = 50, 100, 300$ meV. Note that although no isotopic effects are present for the reflection probability in the classical picture, isotopic effects do appear in the semi-classical diffraction patterns. The latter is evident when comparing the diffraction patterns for the three isotopes at the same E_{in} . This arises due to the quantization of the final diffraction states that depend themselves on the isotope mass. Despite this consideration, the semi-classical diffraction patterns are qualitatively similar for the range of energies that we consider and for the three isotopes. In all cases, diffraction energy channels are populated up to the maximum allowed value of energy transfer to the parallel components, that is $E_{XY} < E_{\text{in}}$. Classical trajectories deflect continuously as they approach the corrugated potential induced by the W(110) surface; this gives rise to a negligible reflection probability for back-scattering events ($E_{XY} \approx 0$), with the most probable exit channel being that with the maximum allowed value of E_{XY} .

The comparison of the above mentioned semi-classical results with the quantum dynamical ones reveals the importance of quantum effects in this observable. In the same figure, the quantum prediction for the diffraction patterns of wave packets centered at the three different values of E_{in} is also shown. For hydrogen scattering at W(110) with small E_{in} , semiclassical and quantum diffraction patterns look quite different [panel (a)]. Results show that the most probable quantum reflection channel is the back-scattering one. While classical trajectories can be continuously deflected, in the quantum case energy transfer to the in-plane degrees of freedom requires coupling to states with momentum parallel to the surface. Those states are discretized, at odds with what happens in the classical case, which makes the energy transfer less efficient. As the incident energy increases, the relative population of the high-energy diffraction channels with respect to the back-scattered channel increases. For $E_{\text{in}} = 300$ meV, the backscatter channel is no longer the most probable one and a quantum diffraction rainbow is observed⁵⁸. Yet, the differences between the semi-classical and quantum predictions persist.

With respect to isotopic effects, quantum diffraction channels are qualitatively different for the three isotopes. For deuterium, for the lowest energy ($E_{\text{in}} = 50$ meV), back-scattering is still the most probable channel, but its probability is similar to that of the highest-energy channel, being in this sense more classical than H. This approximation to the classical limit is clearer as the incident energy increases. Finally, in the case of tritium, the back-scattered channel is highly suppressed even for the lowest energy considered. On a final note it is worth remarking that although the semi-classical approximation does not match the prediction of the quantum rainbow diffraction pattern⁵⁸, some features of the classical patterns remain in the quantum ones. Notably, in the classical picture, some diffraction channels have vanishing probability that arises from geometrical focus effects induced by the corrugation of the PES. This is the case of the channel at 34 meV in panel Fig. 5(a),

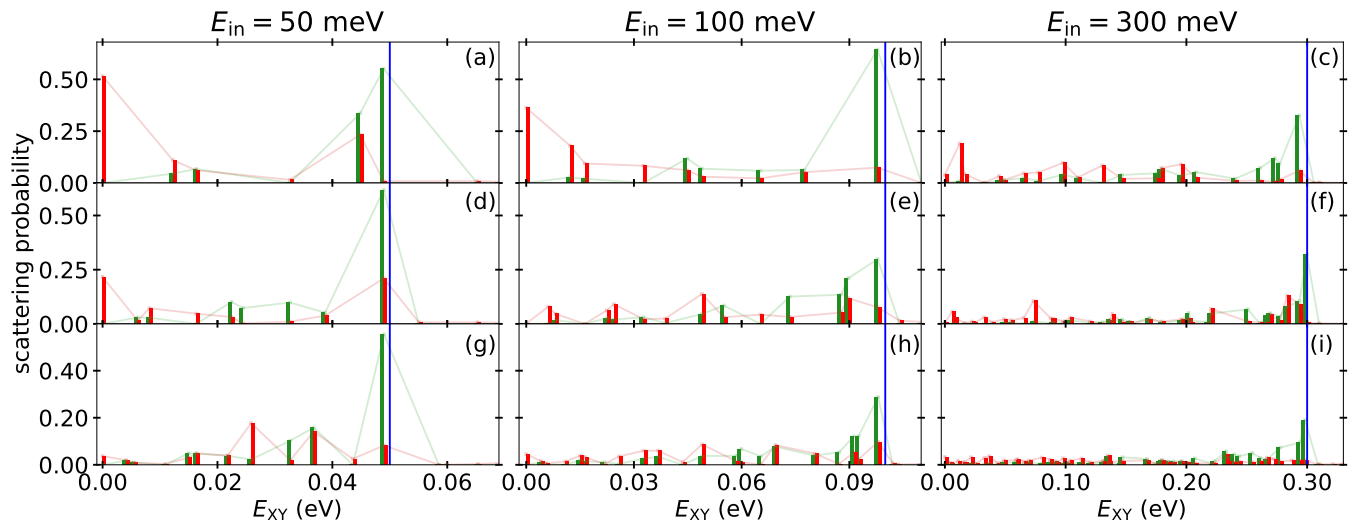


FIG. 5. Energy resolved diffraction probability as a function of energy transfer to parallel (XY) degrees of freedom. Classical (quantum) results are shown by green (red) bars. Panels (a)-(c), (d)-(f), and (g)-(i) show results for hydrogen, deuterium, and tritium isotopes, respectively. The blue vertical lines indicate the values of the incident energy labeled at the top of each column. Since diffraction channels are discrete, the lines serve only as visual guides.

whose vanishing value would be in principle from geometric origin and not due to destructive interference.

IV. SUMMARY

We have studied the scattering of hydrogen isotopes on the W(110) surface using both classical and quantum methods, which allows us to elucidate the role of quantum effects. For hydrogen, the quantum and classical predictions of the absorption probability as a function of the incident energy are in reasonably good agreement for $E_{in} > 200$ meV. At lower incident energies, the quantum dynamical treatment predicts that the absorption curve is dominated by resonances. Consequently, the classical approach is unable to reproduce the quantum results. We show that the origin of these resonances can qualitatively be explained in terms of selective adsorption resonances and diffraction-mediated selective adsorption resonances. This interpretation is further supported by comparing the absorption curves for the three hydrogen isotopes. Our results confirm that the classical limit shifts toward smaller values of E_{in} as the isotope mass increases. Furthermore, the positions at which resonant structures appear in the sticking curve satisfy the expected mass-dependent relationships of their underlying diffraction and vibrational origin. Despite the persistence of quantum effects in the absorption probability computed at long propagation times, we demonstrate that isotopic effects of genuine quantum mechanical origin can still be identified, that introduce differences in the dynamics of the system. Finally, analysis of the diffraction patterns of reflected trajectories give further insight into the origin of such quantum effects. The classical treatment underestimates the back-scattering probability, that is the dominant channel at low incident energies within the quantum descrip-

tion. This behavior is intimately related to the quantization of states at the surface and explains the reduced adsorption probability predicted by the quantum method compared with the classical one. At higher incident energies, both quantum and semi-classical methods predict the appearance of a quantum diffraction rainbow pattern for all three isotopes, however semi-classical results still depart from the quantum ones.

ACKNOWLEDGMENTS

We acknowledge funding from ADAGIO (Advanced Manufacturing Research Fellowship Programme in the Basque – New Aquitaine Region) from the European Union’s Horizon 2020 research and innovation programme under the Marie Skłodowska Curie cofund Grant Agreement No. 101034379. This work was conducted in the scope of the transborder joint Laboratory QuantumChemPhys: Theoretical Chemistry and Physics at the Quantum Scale (ANR-10-IDEX-03-02). Computer time was provided by the Pôle Modélisation HPC facility of the Institut des Sciences Moléculaires, UMR 5255, CNRS, Université de Bordeaux, cofunded by the Nouvelle Aquitaine region as well as the MCIA (Mésocentre de Calcul Intensif Aquitain).

DATA AVAILABILITY STATEMENT

The data that support the findings of this study are available from the corresponding author upon reasonable request.

Appendix A: Vibrational spectra at the surface

We evaluate the bound states of H isotopes on the W(110) surfaces's primitive cell, making use of the improve relaxation algorithm. Table III depicts the vibrational energies of H isotopes adsorbed a the W(110) surface. For each isotope, the energy reference is taken as the one of its ground state. Those ground states for H, D and T have zero point energies (ZPE) of 175 meV, 124 meV and 102 meV, respectively. Notice that these energies satisfy the expected relation for an harmonic potential, $E_{\text{ZPE}}^i = E_{\text{ZPE}}^{\text{H}} \sqrt{m_{\text{H}}/m_i}$ with $i = \text{D, T}$. The corresponding ground state density for H, centered at Hollow position, is depicted in Fig. 6(a). In the primitive cell, two hollow positions are present, and, thus the ground states are doubly degenerated.

The first excitations in the system correspond to vibrational excitations in x and y degrees of freedom. In the case of H, two quasi-degenerate excitations appear for each of the degrees of freedom, corresponding to symmetric, antisymmetric wave functions. As the density in such quasi-degenerated states is barely distinguishable, in Fig 6 we only show the density corresponding to the symmetric cases [see panels (b) and (c)] for the H case. The small splitting between this states arises due to the delocalization of H at hollow position, that allows it to explore the anharmonic region of the well even for these low energy excitations. With our numerical precision, we consider two states to be degenerated if their difference is less than 1 meV. With this criteria, for the cases of D and T, these first vibrational excitations are doubly degenerated. This is in agreement with the fact that D and T states are more localized and thus the spectra becomes more classical. Notice that this first vibrational excitations for the three isotopes do not satisfy the relation $E_{\text{vib}}^i = E_{\text{vib}}^{\text{H}} \sqrt{m_{\text{H}}/m_i}$ with $i = \text{D, T}$ that is expected for the states in an harmonic oscillator potential. This tells us that PES at the W(110) surface becomes anharmonic for energies larger than 250 meV

For higher excitation energies, the density of states increases rapidly and the SB and LB positions start to be populated as $E_{\text{vib}} > 100$ meV. On the contrary, the repulsive atop positions remain unpopulated at these low energies. The density of some representative H states in this range of energy is illustrated in panels (d) - (f), Fig. 6. As it can be seen, as energy grows, first bridge positions are populated, and subsequently a nodal structure appears. The signaling vibrational excitations at that bridge positions also.

TABLE III. Excited state number n , and its energy, E_{vib} , for the first vibrational bound-states of H, D and T at the W(110) surface. The numbers in parenthesis are the corresponding degeneracies.

state number	$E_{\text{vib}}^{\text{H}}$ (meV)	$E_{\text{vib}}^{\text{D}}$ (meV)	$E_{\text{vib}}^{\text{T}}$ (meV)
0	0 (2)	0 (2)	0 (2)
1	81 (1)	63 (2)	52 (2)
2	83 (1)	69 (2)	58 (2)
3	88 (1)	98 (2)	82 (2)
4	91 (1)	99 (2)	98 (2)
5	114 (1)	108 (1)	102(2)
6	118 (1)	109 (1)	115 (2)
7	134 (1)	114 (1)	116 (2)
8	136 (1)	117 (1)	128 (1)
9	147 (1)	126 (1)	129 (1)
10	149 (1)	130 (1)	134 (1)

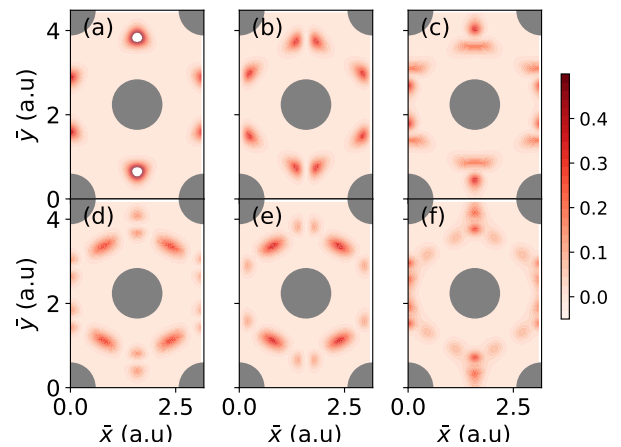


FIG. 6. Cuts of the H nuclear probability density at $Z = 1.1 \text{ \AA}$ for the (a)ground state of H adsorbed at the W(110) surface and for (b)-(f) vibrational states 1, 3, 5, 6 and 7 Table III

¹D. J. Campbell, A. Loarte, D. Boilson, X. Bonnin, P. de Vries, L. Giancarli, Y. Gribov, M. Henderson, S. H. Kim, P. Lamalle, M. Lehnen, T. Luce, I. Nunes, A. R. Polevoi, S. D. Pinches, R. A. Pitts, R. Reichle, M. Schneider, J. Snipes, J. van der Laan, and G. Vayakis, "ITER Research Plan within the Staged Approach (Level III – Final Version)," ITER Technical Report (ITER-24-005) (ITER Organization, 2024).

²J. Bucalossi and *et al.*, "WEST full tungsten operation with an iter grade divertor," Nuclear Fusion **64**, 112022 (2024).

³A. Gallo and *et al.*, "Wall conditions in WEST during operations with a new ITER grade, actively cooled divertor," Nuclear Materials and Energy **41**, 101741 (2024).

⁴C. Maggi and *et al.*, "Overview of T and D–T results in JET with ITER-like wall," Nuclear Fusion **64**, 112012 (2024).

⁵X. Jin, F. Djurabekova, E. A. Hodille, S. Markelj, and K. Nordlund, "Anal-

ysis of lattice locations of deuterium in tungsten and its application for predicting deuterium trapping conditions," Phys. Rev. Mater. **8**, 043604 (2024).

⁶E. H. *et al.*, "Modelling fuel retention in the W divertor during the D/H/D changeover experiment in WEST," Nuclear Materials and Energy **45**, 101999 (2025).

⁷H. F. Busnengo and A. E. Martínez, "H₂ Chemisorption on W(100) and W(110) Surfaces," The Journal of Physical Chemistry C **112**, 5579–5588 (2008), <https://doi.org/10.1021/jp711053c>.

⁸N. Hertl, R. Martin-Barrios, O. Galparsoro, P. Larrégaray, D. J. Auerbach, D. Schwarzer, A. M. Wodtke, and A. Kandratsenka, "Random force in molecular dynamics with electronic friction," The Journal of Physical Chemistry C **125**, 14468–14473 (2021), <https://doi.org/10.1021/acs.jpcc.1c03436>.

⁹R. Martin-Barrios, N. Hertl, O. Galparsoro, A. Kandratsenka, A. M. Wodtke, and P. Larrégaray, "H atom scattering from W(110): A benchmark for molecular dynamics with electronic friction," Phys. Chem. Chem. Phys. **24**, 20813–20819 (2022).

¹⁰O. Bünermann, H. Jiang, Y. Dorenkamp, A. Kandratsenka, S. M. Janke, D. J. Auerbach, and A. M. Wodtke, "Electron-hole pair excitation determines the mechanism of hydrogen atom adsorption," Science **350**, 1346–1349 (2015).

¹¹Y. Dorenkamp, H. Jiang, H. Köckert, N. Hertl, M. Kammler, S. M. Janke, A. Kandratsenka, A. M. Wodtke, and O. Bünermann, "Hydrogen collisions with transition metal surfaces: Universal electronically nonadiabatic

- adsorption," *The Journal of Chemical Physics* **148**, 034706 (2018).
- ¹²R. Martín Barrios, O. Galparsoro, A. Martínez Mesa, L. Uranga-Piña, C. Crespos, and P. Larregaray, "Translational Inelasticity of Hydrogen Atoms Scattering off Hydrogen-Covered W(110) Surfaces," *The Journal of Physical Chemistry C* **125**, 14075–14081 (2021), <https://doi.org/10.1021/acs.jpcc.1c03211>.
 - ¹³R. Martín Barrios, N. Omar, O. Galparsoro, C. Crespos, and P. Larregaray, "Specular scattering of h atoms off pristine and h-covered tungsten surfaces," *The Journal of Physical Chemistry C* **128**, 13333–13338 (2024), <https://doi.org/10.1021/acs.jpcc.4c03231>.
 - ¹⁴N. Hertl, A. Kandratsenka, and A. M. Wodtke, "Effective medium theory for bcc metals: electronically non-adiabatic H atom scattering in full dimensions," *Phys. Chem. Chem. Phys.* **24**, 8738–8748 (2022).
 - ¹⁵S. Yang, S. Kim, and T. Oda, "Sticking, reflection, and abstraction behavior of hydrogen irradiated on (110) tungsten surfaces at 0.1–100 eV by molecular dynamics simulations using a machine learning potential," *Acta Materialia* **297**, 121306 (2025).
 - ¹⁶C. I. Becerra, C. Crespos, O. Galparsoro, and P. Larregaray, "Atomic scattering of H and N on W(100): Effect of lattice vibration and electronic excitations on the dynamics," *Surface Science* **701**, 121678 (2020).
 - ¹⁷R. M. Barrios, O. Galparsoro, A. M. Mesa, L. U. Piña, C. Crespos, and P. Larregaray, "Inelastic scattering of hydrogen atoms off pristine and hydrogen-covered W(100) surfaces," *The European Physical Journal Special Topics* **232**, 1985–1993 (2023).
 - ¹⁸P. Ferrin, S. Kandoi, A. U. Nilekar, and M. Mavrikakis, "Hydrogen adsorption, absorption and diffusion on and in transition metal surfaces: A DFT study," *Surface Science* **606**, 679–689 (2012).
 - ¹⁹O. Bünermann, A. Kandratsenka, and A. M. Wodtke, "Inelastic scattering of H atoms from surfaces," *J. Phys. Chem. A* **125**, 3059–3076 (2021).
 - ²⁰A. J. H. M. Meijer, A. J. Farebrother, D. C. Clary, and A. J. Fisher, "Time-Dependent Quantum Mechanical Calculations on the Formation of Molecular Hydrogen on a Graphite Surface via an Eley-Rideal Mechanism," *The Journal of Physical Chemistry A* **105**, 2173–2182 (2001), <https://doi.org/10.1021/jp003839+>.
 - ²¹M. Persson and B. Jackson, "Flat surface study of the Eley-Rideal dynamics of recombinative desorption of hydrogen on a metal surface," *The Journal of Chemical Physics* **102**, 1078–1093 (1995).
 - ²²B. Jackson and M. Persson, "Effects of isotopic substitution on Eley-Rideal reactions and adsorbate-mediated trapping," *The Journal of Chemical Physics* **103**, 6257–6269 (1995).
 - ²³E. Pijper, G. J. Kroes, R. A. Olsen, and E. J. Baerends, "The effect of corrugation on the quantum dynamics of dissociative and diffractive scattering of H₂ from Pt(111)," *The Journal of Chemical Physics* **113**, 8300–8312 (2000).
 - ²⁴G.-J. Kroes, "Six-dimensional quantum dynamics of dissociative chemisorption of H₂ on metal surfaces," *Progress in Surface Science* **60**, 1–85 (1999).
 - ²⁵E. Pijper, M. Somers, G. Kroes, R. Olsen, E. Baerends, H. Busnengo, A. Salin, and D. Lemoine, "Six-dimensional quantum dynamics of scattering of ($v=0, j=0$) H₂ from Pt(111): comparison to experiment and to classical dynamics results," *Chemical Physics Letters* **347**, 277–284 (2001).
 - ²⁶C. Díaz, M. F. Somers, G. J. Kroes, H. F. Busnengo, A. Salin, and F. Martín, "Quantum and classical dynamics of H₂ scattering from Pd(111) at off-normal incidence," *Phys. Rev. B* **72**, 035401 (2005).
 - ²⁷C. Díaz, R. A. Olsen, D. J. Auerbach, and G. J. Kroes, "Six-dimensional dynamics study of reactive and non reactive scattering of H₂ from Cu(111) using a chemically accurate potential energy surface," *Phys. Chem. Chem. Phys.* **12**, 6499–6519 (2010).
 - ²⁸L. Xiong, L. Zhang, B. Zhao, and B. Jiang, "Six-dimensional quantum dynamics of an Eley-Rideal reaction between gaseous and adsorbed hydrogen atoms on Cu(111)," *Faraday Discuss.* **251**, 457–470 (2024).
 - ²⁹L. Xiong and B. Jiang, "Comparison of Six-Dimensional Quantum and Quasi-Classical Dynamics of the Eley-Rideal Reaction of H(D) Atoms with D(H)-Covered Cu(111)," *J. Phys. Chem. C* **128**, 9003–9010 (2024), <https://doi.org/10.1021/acs.jpcc.4c01571>.
 - ³⁰L. Shi, M. Schröder, H.-D. Meyer, D. Peláez, A. M. Wodtke, K. Golibrzuch, A.-M. Schönemann, A. Kandratsenka, and F. Gatti, "Quantum and classical molecular dynamics for H atom scattering from graphene," *The Journal of Chemical Physics* **159**, 194102 (2023).
 - ³¹L. Shi, M. Schröder, H.-D. Meyer, D. Peláez, A. M. Wodtke, K. Golibrzuch, A.-M. Schönemann, A. Kandratsenka, and F. Gatti, "Full Quantum Dynamics Study for H Atom Scattering from Graphene," *The Journal of Physical Chemistry A* **129**, 1896–1907 (2025).
 - ³²X. Sha, B. Jackson, and D. Lemoine, "Quantum studies of Eley-Rideal reactions between H atoms on a graphite surface," *The Journal of Chemical Physics* **116**, 7158–7169 (2002).
 - ³³H. Jiang, X. Tao, M. Kammler, F. Ding, A. M. Wodtke, A. Kandratsenka, T. F. I. Miller, and O. Bünermann, "Small Nuclear Quantum Effects in Scattering of H and D from Graphene," *The Journal of Physical Chemistry Letters* **12**, 1991–1996 (2021), <https://doi.org/10.1021/acs.jpcclett.0c02933>.
 - ³⁴B. Lepetit, D. Lemoine, Z. Medina, and B. Jackson, "Sticking and desorption of hydrogen on graphite: A comparative study of different models," *The Journal of Chemical Physics* **134**, 114705 (2011).
 - ³⁵M. S. Gravielle and J. E. Miraglia, "Semiquantum approach for fast atom diffraction: Solving the rainbow divergence," *Phys. Rev. A* **90**, 052718 (2014).
 - ³⁶A. S. Muzas, L. Frisco, G. A. Bocan, C. D'iaz, and M. S. Gravielle, "Semiquantum versus quantum methods for grazing-incidence fast-atom diffraction: Influence of the wave-packet size," *Phys. Rev. A* **109**, 042823 (2024).
 - ³⁷G. A. Bocan, H. Breiss, S. Szilasi, H. Momeni, E. M. S. Casagrande, M. S. Gravielle, E. A. Sánchez, and H. Khemliche, "Anomalous KCl(001) Surface Corrugation from Fast He Diffraction at Very Grazing Incidence," *Phys. Rev. Lett.* **125**, 096101 (2020).
 - ³⁸R.-H. Bi and W. Dou, "Electronic friction near metal surface: Incorporating nuclear quantum effect with ring polymer molecular dynamics," *J. Chem. Phys.* **160**, 074110 (2024).
 - ³⁹O. Bridge, P. Lazzaroni, R. Martinazzo, M. Rossi, S. C. Althorpe, and Y. Litman, "Quantum rates in dissipative systems with spatially varying friction," *J. Chem. Phys.* **161**, 024110 (2024).
 - ⁴⁰J. Chen, J. Lee, and W. Dou, "How to correct Ehrenfest nonadiabatic dynamics in open quantum systems: Ehrenfest plus random force ($E + \sigma$) dynamics," *J. Chem. Phys.* **162**, 044104 (2025).
 - ⁴¹R. J. Preston, Y. Ke, S. L. Rudge, N. Hertl, R. Borrelli, R. J. Maurer, and M. Thoss, "Nonadiabatic quantum dynamics of molecules scattering from metal surfaces," *J. Chem. Theory Comput.* **21**, 1054–1063 (2025), <https://doi.org/10.1021/acs.jctc.4c01586>.
 - ⁴²O. Galparsoro, R. Pétuya, F. Busnengo, J. I. Juaristi, C. Crespos, M. Alducin, and P. Larregaray, "Hydrogen abstraction from metal surfaces: when electron-hole pair excitations strongly affect hot-atom recombination," *Phys. Chem. Chem. Phys.* **18**, 31378–31383 (2016).
 - ⁴³R. Pétuya, C. Crespos, E. Quintas-Sanchez, and P. Larregaray, "Comparative Theoretical Study of H₂ Eley-Rideal Recombination Dynamics on W(100) and W(110)," *The Journal of Physical Chemistry C* **118**, 11704–11710 (2014), <https://doi.org/10.1021/jp501679n>.
 - ⁴⁴H. F. Busnengo, A. Salin, and W. Dong, "Representation of the 6D potential energy surface for a diatomic molecule near a solid surface," *The Journal of Chemical Physics* **112**, 7641–7651 (2000).
 - ⁴⁵R. A. Olsen, H. F. Busnengo, A. Salin, M. F. Somers, G. J. Kroes, and E. J. Baerends, "Constructing accurate potential energy surfaces for a diatomic molecule interacting with a solid surface: H₂+Pt(111) and H₂+Cu(100)," *The Journal of Chemical Physics* **116**, 3841–3855 (2002).
 - ⁴⁶M. Beck, A. Jäckle, G. Worth, and H.-D. Meyer, "The multiconfiguration time-dependent Hartree (MCTDH) method: a highly efficient algorithm for propagating wavepackets," *Phys. Rep.* **324**, 1–105 (2000).
 - ⁴⁷A. Jäckle and H. Meyer, "Product representation of potential energy surfaces," *The Journal of Chemical Physics* **104**, 7974–7984 (1996).
 - ⁴⁸G. Henkelman, B. P. Uberuaga, and H. Jónsson, "A climbing image nudged elastic band method for finding saddle points and minimum energy paths," *The Journal of Chemical Physics* **113**, 9901–9904 (2000).
 - ⁴⁹H.-D. Meyer, F. Le Quéré, C. Léonard, and F. Gatti, "Calculation and selective population of vibrational levels with the Multiconfiguration Time-Dependent Hartree (MCTDH) algorithm," *J. Chem. Phys.* **329**, 179–192 (2006).
 - ⁵⁰J. M. Moix and E. Pollak, "Semiclassical initial-value-representation study of helium scattering from Cu(110)," *Phys. Rev. A* **79**, 062507 (2009).
 - ⁵¹Z. Medina and B. Jackson, "Quantum studies of light particle trapping, sticking, and desorption on metal and graphite surfaces," *The Journal of Chemical Physics* **128**, 114704 (2008).
 - ⁵²V. Bortolani and A. C. Levi, "Atom-surface scattering theory," *La Rivista del Nuovo Cimento* **9**, 1–77 (1986).
 - ⁵³A. Sanz and S. Miret-Artés, "Selective adsorption resonances: Quantum

- and stochastic approaches,” *Physics Reports* **451**, 37–154 (2007).
- ⁵⁴L. Bonnet, C. Crespos, and M. Monnerville, “Chemical reaction thresholds according to classical-limit quantum dynamics,” *J. Chem. Phys.* **157**, 094114 (2022).
- ⁵⁵S. Miret-Artés and J. R. Manson, “Focused sticking of light mass particles in physisorption,” *Phys. Rev. B* **63**, 121404 (2001).
- ⁵⁶G. Benedek, G. Brusdeylins, J. P. Toennies, and R. B. Doak, “Experimental evidence for kinematical focusing in the inelastic scattering of helium from the NaF(001) surface,” *Phys. Rev. B* **27**, 2488–2493 (1983).
- ⁵⁷A. Rodríguez-Fernández, L. Bonnet, C. Crespos, P. Larrégaray, and R. Díez Muiño, “When Classical Trajectories Get to Quantum Accuracy: The Scattering of H₂ on Pd(111),” *J. Phys. Chem. Lett.* **10**, 7629–7635 (2019), <https://doi.org/10.1021/acs.jpcclett.9b02742>.
- ⁵⁸S. Miret-Artés and E. Pollak, “Classical theory of atom–surface scattering: The rainbow effect,” *Surf. Sci. Reports* **67**, 161–200 (2012).